Nuclear Instruments and Methods in Physics Research A 729 (2013) 307–315

Contents lists available at ScienceDirect

Nuclear Instruments and Methods in Physics Research A

journal homepage: www.elsevier.com/locate/nima

On the response of a europium doped phosphor-coated CMOS digital imaging detector

I.E. Seferis [a], C.M. Michail [b], I.G. Valais [b], G.P. Fountos [b], N.I. Kalyvas [b], F. Stromatia [c], G. Oikonomou [d], I.S. Kandarakis [b,*], G.S. Panayiotakis [a]

[a] Department of Medical Physics, Faculty of Medicine, University of Patras, 26500 Patras, Greece
[b] Department of Medical Instruments Technology, Technological Educational Institute (TEI) of Athens, Agios Spyridonos, 12210 Athens, Greece
[c] Department of Radiology and Nuclear Medicine, "IASO" General Hospital, Mesogion 264, 15562 Holargos, Greece
[d] Department of Medical Radiological Technology, Faculty of Health and Caring Professions, Technological Educational Institute (TEI) of Athens, Agios Spyridonos, 12210 Athens, Greece

ARTICLE INFO

Article history:
Received 22 February 2013
Received in revised form
20 May 2013
Accepted 27 June 2013
Available online 19 July 2013

Keywords:
CMOS detector
Image quality
Scintillating detectors

ABSTRACT

Purpose: The purpose of the present study was to assess the information content of a high resolution active pixel CMOS imaging sensor coupled to Gd_2O_2S:Eu phosphor screens in terms of single index image quality metrics such as the information capacity (IC) and the noise equivalent passband (Ne).
Methods: The CMOS sensor was coupled to two Gd_2O_2S:Eu scintillator screens with coating thicknesses of 33.3 and 65.1 mg/cm^2. IC and Ne were obtained by means of experimentally determined parameters such as the modulation transfer function (MTF), the detective quantum efficiency (DQE) and the noise equivalent quanta (NEQ). Measurements were performed using the standard IEC-RQA5 radiation beam quality (70 kVp) and a W/Rh beam quality (28 kVp).
Results: It was found that the detector response function was linear for the exposure ranges under investigation. At 70 kVp, under the RQA 5 conditions IC values were found to range between 1730 and 1851 bits/mm^2 and Ne values were found between 2.28 and 2.52 mm^{-1}. At 28 kVp the corresponding IC values were found to range between 2535 and 2747 bits/mm^2, while the Ne values were found between 5.91 and 7.09 mm^{-1}.
Conclusion: IC and Ne of the red emitting phosphor/CMOS sensor combination were found with high values suggesting an acceptable imaging performance in terms of information content and sharpness, for X-ray digital imaging.

1. Introduction

The development of new digital diagnostic imaging techniques and modalities, such as digital breast tomosynthesis (DBT) [1], dual energy (DE) imaging [2], scanning slot digital mammography detectors [3], energy selective techniques [4,5] and digital fluoroscopy systems [6], require efficient scintillators to reduce patient dose. Digital imaging systems with smaller sizes for the detector elements (dels) are also required to improve image resolution and the visibility of microcalcifications, without noise increase and DQE degradation. Many Si photodetectors show very high or excellent quantum efficiency (QE) in the red wavelength range [7–14]. Due to this property the performance of red emitting phosphors [13,15–17] and in particular, of the europium (Eu^{3+}) activated Gd_2O_2S has been investigated in terms of optical output [15], emission efficiency [18–21] and imaging performance [12,18–20]. Such phosphors are cost effective and can be easily prepared by inserting europium ion activator (Eu^{3+}) in rare earth based host matrices. In addition europium-activated phosphors have a decay time of the order of one millisecond (slightly higher than Gd_2O_2S:Tb) which is acceptable for applications that do not involve high framing rates [22,23]. These include digital radiography, and mammography. Gd_2O_2S:Eu has been previously employed in single pulse dual energy radiography [24], in digital mammography and diffraction enhanced breast imaging with CCD arrays [25–28]. Furthermore Gd_2O_2S:Eu has been previously used as phosphor insert in phantoms for limited-angle X-ray luminescence tomography (XLT) [29] and hybrid X-ray luminescence/optical imaging [30]. Previously, the image quality of a detector based on a commercial Gd_2O_2S:Tb screen coupled to an active CMOS sensor has been investigated by our group [31]. In the present study this CMOS sensor was coupled to two custom made Gd_2O_2S:Eu phosphor

* Corresponding author. Tel.: +30 210 5385387.
E-mail address: kandarakis@teiath.gr (I.S. Kandarakis).

0168-9002/$ - see front matter © 2013 Elsevier B.V. All rights reserved.
http://dx.doi.org/10.1016/j.nima.2013.06.107

screens, prepared in our laboratory, and the whole detector was evaluated under 70 kVp (general radiography) and 28 kVp (mammography) X-ray spectra.

The information content of the detector under investigation was achieved by the assessment of single index metrics such as the noise equivalent passband and the information capacity. These two indices are based on integration of spatial frequency dependent parameters such as the modulation transfer function (MTF), the detective quantum efficiency (DQE) and the noise equivalent quanta (NEQ). Although none of these measures is directly related to the diagnostic yield in image interpretation, they are commonly used as physical measures that are useful in comparing different systems.

The experimental method was based on the guidelines published by the International Electrotechnical Commission (IEC) [32], which has standardized the methodology for measuring DQE in digital detectors. In addition the results of the present work have been compared with the results of previously studied CMOS sensors coupled to Gd_2O_2S:Tb phosphor screens [31,33].

2. Materials and methods

2.1. Phosphor screen preparation

The Gd_2O_2S:Eu phosphor employed in the present study, was purchased in powder form (Phosphors Technology Ltd, England, code UKL63/N-R1) with mean grain size of approximately 8 μm and volume density of 7.3 g/cm^3. The phosphor was used in the form of thin layers (test screens) to simulate the intensifying screen employed in X-ray mammography and radiography. The screens were prepared by sedimentation [34] of the powder phosphors on borosilicate glass substrate, with no reflective layer, and thickness of approximately 0.14 mm (Waldemar Knittel-GmbH). The coating thicknesses of the two screens correspond to 33.3 mg/cm^2 for mammography, and 65.1 mg/cm^2 for radiography, (91.2 and 178.3 μm assuming a 50% packing density) respectively [35,36].

2.2. CMOS sensor and experimental setup

For the detector under investigation, two Gd_2O_2S:Eu phosphor screens, with coating thicknesses of 33.3 mg/cm^2, for mammography, and 65.1 mg/cm^2, for radiography, were manually coupled to an optical readout device including a CMOS Remote RadEye HR photodiode pixel array [37]. The CMOS photodiode array consists of 1200 × 1600 pixels with 22.5 μm pixel spacing and a fill factor of 0.8 [31]. To avoid light photons interactions with the glass substrate, the experiments were performed with the phosphor layer directly overlaid onto the active area of the CMOS photodiode array, consisting of an n-well diffusion on p-type epitaxial silicon, and held by using a thin polyurethane foam layer for compression between the screen and a 1 mm thick graphite cover. A component view is shown in Fig. 1. Experiments, on the CMOS optical sensor, were carried out in both X-ray mammography and radiography energy ranges. Two beam qualities were used; 28 kV W/Rh for mammography and 70 kV (RQA 5) for radiography according to the IEC standards [31]. IEC standards X-ray spectra were achieved by adding 2 mm Al and 21 mm Al filtration respectively. Half value layers were calculated and found 7.1 mm Al for RQA 5 and 0.77 mm Al for W/Rh conditions respectively.

2.3. X-ray spectra measurement

A Hologic Selenia X-ray tube was used for the W/Rh beam quality [38] and a Del Medical Eureka X-ray tube with a rotating tungsten anode and 1.5 mm aluminum (Al) inherent filtration for the RQA 5 beam quality [39].

In this study the source-to-detector distances (SDD) between the X-ray focal spot and the surface of the detector was set to 185 and 66 cm for the radiographic and mammographic energies, respectively [32]. The added filtration was placed as close as possible to the source.

A portable Amptek XR-100T X-ray spectrometer [40], based on a cadmium telluride (CdTe) crystal solid-state detector was used for direct diagnostic X-ray spectra measurements [41]. After calibration [31] the CdTe was placed at a focus to detector distance of 166 and 48 cm for the radiographic and the mammographic energies respectively. X-ray spectra were corrected by the inverse square law at the CMOS detector plane for all beam qualities. In order to minimize pile-up distortions, dedicated collimation systems (1 mm thick collimators with 400 μm and 100 μm diameters, respectively for the RQA 5 and W/Rh X-ray spectra) were used. In addition the measured X-ray spectra were corrected for the efficiency of the CdTe detector. The air kerma value K_α at the surface of the detector was calculated according to [41]

$$K_\alpha = 0.00869 \times \sum_{E\min}^{E_0} (1.83 \times 10^{-6} \times \Phi_0(E) \times E \times (\mu_{en}(E)/\rho)_{air}) \quad (1)$$

where Φ_0 is the measured X-ray spectrum value (photons/mm^2) at energy E. $(\mu_{en}(E)/\rho)_{air}$ is the X-ray mass energy absorption coefficient of air at energy E obtained from the literature [42]. The exposure rate at the entrance surface of the CMOS photodiode array detector was measured for a range of tube current-time products (mAs). The measured X-ray spectra were corrected for the efficiency of the CdTe detector.

2.4. Imaging performance

2.4.1. Signal transfer property (STP)

The signal transfer property (STP), or detector response, states the relationship between mean pixel value (MPV) and entrance surface air kerma (ESAK). This relationship was obtained by plotting pixel values (PV) versus ESAK at the detector, as described in the IEC method [32]. A sequence of uniform images was acquired at different exposure levels. MPV was evaluated in a 1 × 1 cm region of interest (ROI). The mean pixel value (MPV) and the standard deviation within that region were measured. The system's response curve was fitted using a linear equation of the form

$$\mathrm{MPV} = \alpha + b \times K_\alpha \quad (2)$$

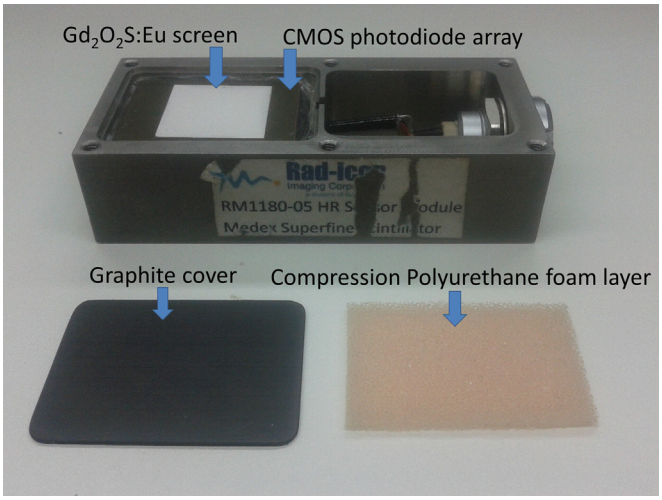

Fig. 1. Gd_2O_2S:Eu screen coupled to RadEye HR CMOS sensor.

where α and b are fit parameters. From the slope of the system's response curve, the value of the gain factor (G) was obtained. This value is relating MPV to the incident exposure at the detector (in digital units per μGy) [43]. The magnitude of the pixel offset at zero air kerma was also estimated [44].

2.4.2. Spatial frequency dependent image quality parameters

2.4.2.1. Modulation transfer function (MTF). The MTF was measured using the slanted-edge technique, following the procedures described in IEC standard [45–47]. A tungsten edge test device, was supplied by the PTW Freiburg Company, was used to obtain the slanted edge images in both RQA 5 and W/Rh conditions. The edge test device consists of a 1 mm thick W edge plate (100×75 mm^2) fixed on a 3 mm thick lead plate. Images of the edge, placed at a slight angle, were obtained under the radiographic and mammographic imaging conditions. Three exposure levels have to be chosen for the measurements. From these levels, the medium one should be the 'normal' level routinely employed in the clinical practice [32–48]. The edge spread function (ESF) was calculated by the extraction of a 1×1 cm^2 ROI with the edge roughly at the center. The angle of the edge was then determined using a simple linear least squares fit and the 2D image data were re-projected around the angled edge [45] to form an ESF with a bin spacing of 0.1 pixels. The ESF was smoothed with a median filter of five bins to reduce high frequency noise. The median filter is much less sensitive to extreme values (outliers) than averaging filters. Therefore it is more efficient to remove these outliers without reducing the sharpness of the image. Then the ESF was differentiated to obtain the line spread function (LSF) [42,49]. Finally, the normalized LSF was Fourier transformed to give the pre-sampling MTF.

2.4.2.2. Normalized noise power spectrum (NNPS). The NPS was calculated according to IEC 62220-1-2 [32]. For each ROI, the PV were converted into air kerma units with Eq. (2). The slowly varying spatial background effects including the heel effect were corrected by fitting and subtracting a two-dimensional second-order polynomial to the original acquired image data. The area of analysis was subsequently divided into sub-images of 1024×1024 pixels. Half overlapping ROIs with a size of 128×128 pixels were then taken from the sub-images [32]. A total of 128 ROIs were taken from each flood image. For all the ROIs taken from each image 2D fast Fourier transform (FFT) of each ROI was calculated and added to the NPS ensemble. NNPS was obtained by dividing NPS by the square of the corresponding K_α and afterward the ensemble average was obtained.

2.4.2.3. Detective quantum efficiency (DQE). The DQE of the system was calculated by the following equation:

$$\mathrm{DQE}(u) = \frac{\mathrm{MTF}^2(u)}{K_\alpha \times q \times \mathrm{NNPS}(u)} \tag{3}$$

where q is the number of photons per unit kerma (μGy) per mm^2, determined by dividing the number of photons per mm^2 (measured with the portable X-ray spectrometer) with the corresponding air kerma value (μGy) [41]. Values of 21,738 photons $\times$ μGy^{-1} $\times$ mm^{-2}, for the RQA 5, and 5422 photons $\times$ μGy^{-1} $\times$ mm^{-2}, for W/Rh beam qualities, were calculated from our direct X-ray spectra measurements, instead of using tabulated data.

2.4.2.4. Noise equivalent quanta (NEQ). A measure of the lower number of exposure quanta required by an ideal detector to yield the same SNR^2_{out} as the practical detector working at a given exposure level can be expressed by the noise equivalent quanta (NEQ) [50]. The latter is the combined effects of signal and noise, in terms of spatial frequency. Also it provides an index of the signal-to-noise ratio (SNR) associated with the diagnostic value of a medical image. NEQ can be derived by the product of DQE with photon fluence Φ_0, as determined from the measured X-ray spectrum, as follows [46]:

$$\mathrm{NEQ}(u) = \mathrm{DQE}(u) \times \Phi_0 \tag{4}$$

2.4.3. Singe index image quality parameters

2.4.3.1. Information capacity (IC). The concept of image information capacity (IC) has been introduced within the context of Shannon's information theory, in order to assess image information content [51–61]. However, little work relevant to medical imaging has been published up to now [31,56–66].

According to Shannon's information theory, if it is possible to distinguish N_s different signal intensity levels of duration T on a channel, we can say that the channel can transmit $\log_2 N_s$ bits in time T. The rate of transmission is then $\log_2 N_s/T$. More precisely, the image information capacity, per unit of image area, may be defined as follows [67]:

$$\mathrm{IC} = \lim_{T\to\infty} \log_2 N_s/T = n_p \log_2 N_s \tag{5}$$

where n_p is the number of image elements (pixels) per unit of area that can be registered in an image. If the transmitter has a dynamic range (D) and the noise in the transmission channel is assumed to be Gaussian (normal $(0,\sigma^2)$) and independent of the signal amplitude, then an expression may be derived for N_s in terms of D and σ. For this case, the levels are equally spaced between zero and D with a spacing determined by the acceptable error rate for signal transmission. If each level have an interval of $\pm\kappa\sigma$, according to Wagner [64], then the spacing becomes $2\kappa\sigma$, and one obtains: $N_s - 1 = D/2\kappa\sigma$. Eq. (6) may now be written as follows: $\mathrm{IC} = n_p \log_2(1 + D/2\kappa\sigma)$. Shannon showed that in the frequency domain there is a definition of information capacity that is consistent with the equations described above and which serves as a unique upper limit for the rate of information transmission [67]. This upper limit for the number of distinguishable signals in communication channel of bandwidth Δu is defined as: $N_s \le (\sqrt{(\mathrm{SPS}+\mathrm{NPS})/\mathrm{NPS}})^{2T\Delta u}$. SPS is the signal power spectrum which can be defined as: $\mathrm{SPS} = \left(\mathrm{MFT} \times G^2\right)$, where G is the gain factor (in digital units per μGy) [64]. Consequently, the channel capacity is limited by [67]:

$$\mathrm{IC} = \log_2 N_s/T \le \Delta u \log_2((\mathrm{SPS}+\mathrm{NPS})/\mathrm{NPS}) \tag{6}$$

where SPS and NPS are assumed constants over the frequency interval Δu. Wagner has expressed this equation [64] under the following form:

$$\mathrm{IC}(\Delta u) = 2\Delta u \log_2((\mathrm{SPS}+\mathrm{NPS})/\mathrm{NPS})^{1/2} \tag{7}$$

where the exponent of 1/2 is explained since the ratio of amplitudes is replaced by a ratio of powers, and the factor $2\Delta u$results directly from the sampling theorem. For any function having a bandwidth of Δu, sampling at intervals $\Delta u/2$ completely specifies the function. If the function is assumed to be limited to a time interval T, then for a real function there are just $2\Delta uT$independent values of $2\Delta u$values per unit time. The dimensions of *IC* are bits per unit time [64]. If (7) is integrated over the whole frequency range then information capacity is given by

$$\mathrm{IC} = \int_0^u \log_2(1 + \mathrm{SPS}(u)/\mathrm{NPS}(u))du \tag{8}$$

where u is greater than or equal to the band limit of the signal power. The 2D form of (8) is given by $\mathrm{IC} = (2\Delta u_x)(2\Delta u_y)\log_2((\mathrm{SPS}+\mathrm{NPS})/\mathrm{NPS})^{1/2}$, written in terms of spatial frequency, leading similarly to an integral over the upper right-hand quadrant

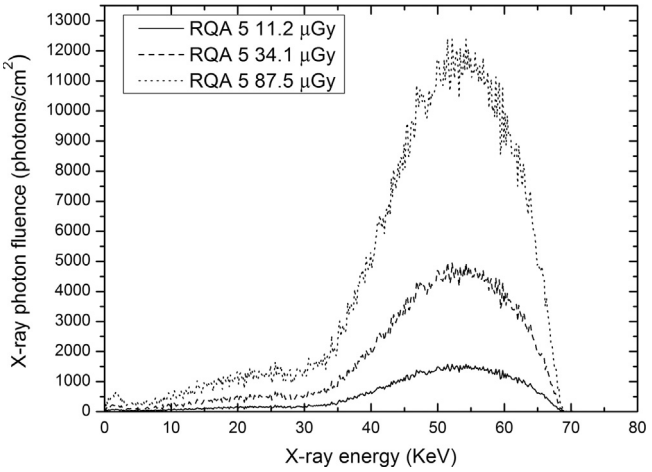

Fig. 2. Measured X-ray spectra for the RQA 5 beam quality.

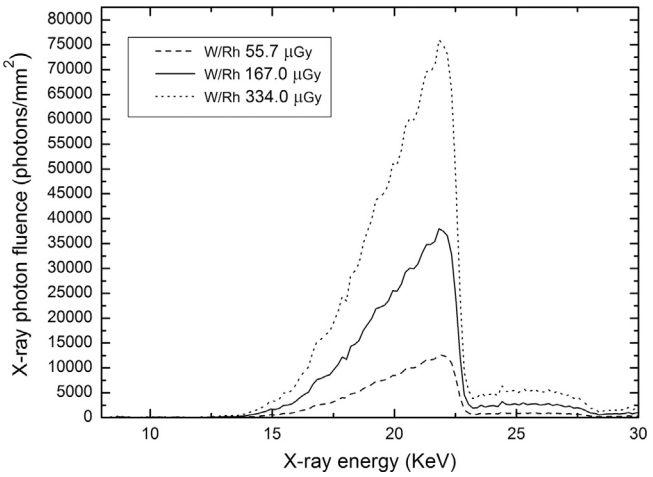

Fig. 3. Measured X-ray spectra for W/Rh beam quality.

inu_x,u_y ($u=(u_x^2+u_y^2)^{1/2}$) space or using polar frequency coordinates and assuming cylindrical symmetry of SPS and NPS, expressed in bits per unit area [64]

$$\mathrm{IC}=\frac{1}{2}\int_0^u \log_2(1+\mathrm{SPS}(u)/\mathrm{NPS}(u))s\pi u du \tag{9}$$

For the detectors used in both conventional and digital X-ray imaging, power spectra can be represented as one-dimensional functions of spatial frequency u, SPS(u) and NPS(u) due to rotational symmetry [64]. Eq. (10) now becomes [56,58–61,64–67]

$$\mathrm{IC}=\pi\int_0^\infty \log_2(1+(\mathrm{SPS}(u)/\mathrm{NPS}(u)))u du \tag{10}$$

where $\mathrm{SPS}(u)/\mathrm{NPS}(u)=\mathrm{NEQ}(u)$, therefore (11) becomes

$$\mathrm{IC}=\pi\int_0^\infty \log_2(1+\mathrm{NEQ}(u))u du \tag{11}$$

2.4.3.2. Noise equivalent passband (Ne). The noise equivalent passband expressing the image sharpness by a single number and has been defined by the relation [60]

$$\mathrm{Ne}=2\int_0^\infty \mathrm{MTF}^2(u)du \tag{12}$$

Different systems with the same Ne are equivalent to white noise, that is, noise represented with the same amplitude to all frequencies.

Table 1
Parameters of the RQA 5 and W/Rh beam qualities.

Radiation beam parameters	Mammographic quality (W/Rh)	Radiographic quality (RQA 5)
Anode/filtration combination	W/Rh	W/Al
Tube voltage (kVp)	28	70
Added filtration (mm Al)	2	21
Measured half value layer-HVL (mm Al)	0.77	7.1
q (photons $\times$ μGy^{-1} $\times$ mm^{-2})	5422 ± 53	$21{,}738\pm107$

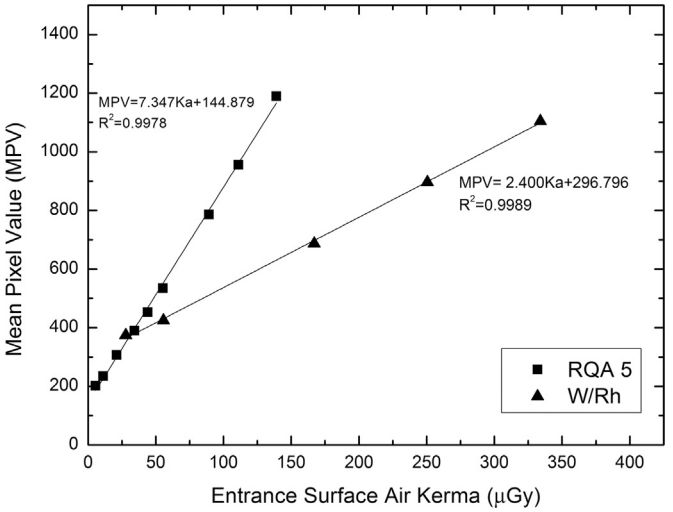

Fig. 4. STP curves of the Gd_2O_2S:Eu based CMOS sensor combined with the 65.1 and 33.3 mg/cm^2 Gd_2O_2S:Eu screens under the RQA 5 and the W/Rh beam qualities, respectively.

3. Results and discussion

Figs. 2 and 3 show measured spectra produced by the X-ray tubes (radiographic with W/Al target-filter combination and mammographic with W/Rh target-filter combinations), used in the present study. The tube settings were: 20, 63 and 157.5 mAs at 70 kVp (RQA 5) and 20, 60 and 120 mAs at 28 kV (W/Rh) respectively. The system reproducibility was verified by measuring X-ray spectra several times. Entrance surface air kerma was calculated by relation (1) using the Amptek XR-100T X-ray spectrometer measurements and was found 11.2 ± 0.020, 34.1 ± 0.045 and 87.5 ± 0.071 μGy for the RQA 5 and 55.7 ± 0.036, 167.0 ± 0.064 and 334.0 ± 0.093 μGy for W/Rh conditions. In Table 1 the parameters for the X-ray spectra used, as well as the measured HVL and q values are shown.

Fig. 4 shows the relationship between mean pixel values and entrance surface air kerma providing the detector response curves (STP) of the Gd_2O_2S:Eu based CMOS sensor combined with the 65.1 and 33.3 mg/cm^2 GOS:Eu screens under the RQA 5 (70 kVp) and the W/Rh (28 kVp) beam qualities, respectively. The detector was found to have a linear response, covering the whole exposure range, with a pixel value offset of 144.879 for the RQA 5 beam quality and 296.796 for the W/Rh beam quality. The linear no threshold fits gave correlation coefficients (R^2) greater than 0.9978 and 0.9989 for the RQA 5 and the W/Rh beam qualities. The gain factor G was determined as the slope of the characteristic curve, relating the mean pixel value to the incident exposure. Using flat-field images the gain factors were determined by linear regression to be $G=7.347$ digital units per μGy for RQA 5 and 2.400 digital units per μGy for W/Rh.

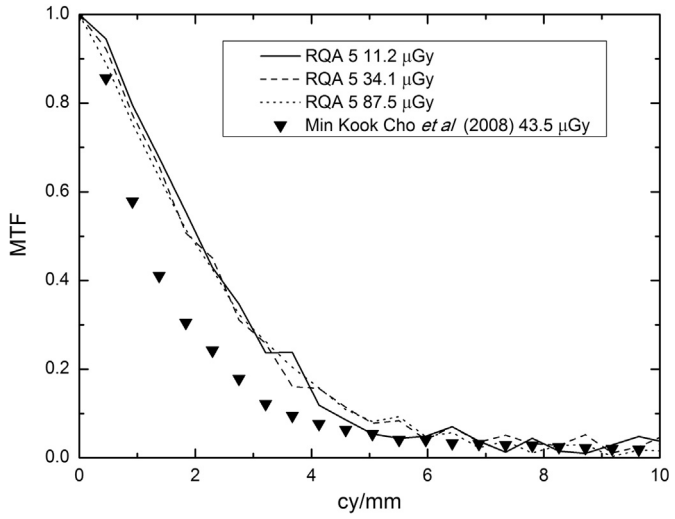

Fig. 5. Comparison of the MTFs of the CMOS/Gd_2O_2S:Eu 65.1 mg/cm^2 sensor under investigation and a previously published CMOS/Gd_2O_2S:Tb 59.2 mg/cm^2 sensor under RQA 5 beam quality.

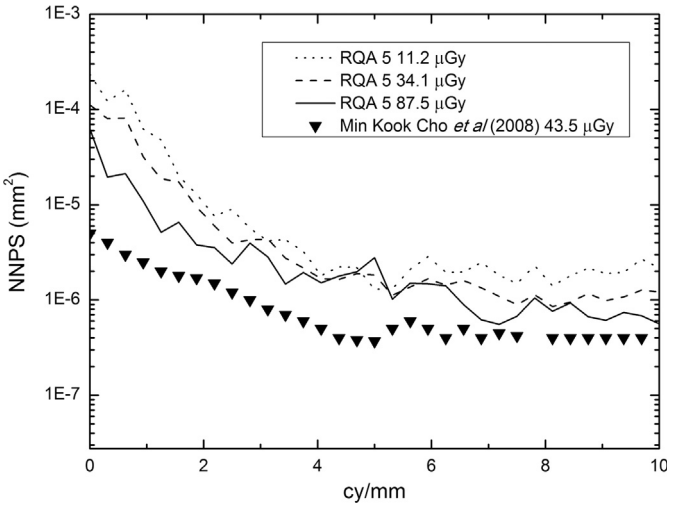

Fig. 7. Comparison of the NNPS curves between the CMOS/Gd_2O_2S:Eu 65.1 mg/cm^2 sensor under investigation and a previously published CMOS/Gd_2O_2S:Tb 59.2 mg/cm^2 sensor under RQA 5 beam quality.

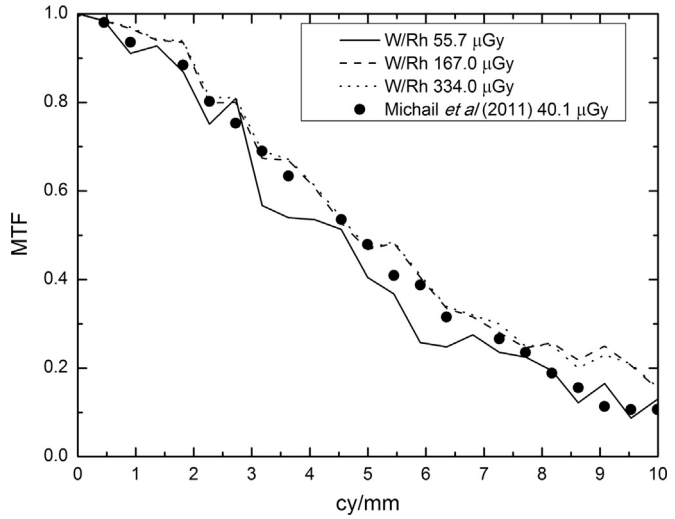

Fig. 6. Comparison of the MTFs for the CMOS/Gd_2O_2S:Eu 33.3 mg/cm^2 sensor under investigation and a previously published CMOS/Gd_2O_2S:Tb 33.9 mg/cm^2 sensor under W/Rh and RQA M2 beam qualities, respectively.

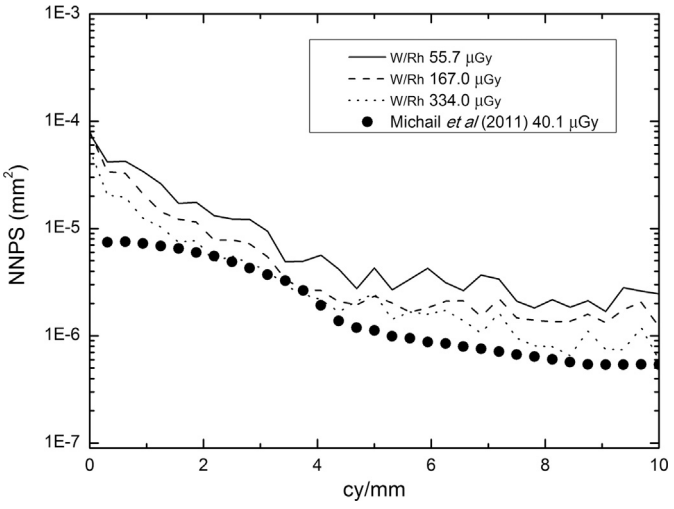

Fig. 8. Comparison of the NNPS curves between the CMOS/Gd_2O_2S:Eu 33.3 mg/cm^2 sensor under investigation and a previously published CMOS/Gd_2O_2S:Tb 33.9 mg/cm^2 sensor under W/Rh and RQA M2 beam qualities, respectively.

Figs. 5 and 6 show the modulation transfer function (MTF) curves for three exposure levels under the RQA5 and W/Rh beam qualities respectively. The standard deviation of all MTF curves was below 2%. In Fig. 5 the MTF of a CMOS sensor with 48 μm pixel pitch coupled to a Gd_2O_2S:Tb screen of 59.2 mg/cm^2 coating thickness [33], is also shown for comparison. This MTF has been obtained under RQA 5 beam quality at 43.5 μGy. As it can be depicted from Fig. 5, the MTF of the 48 μm CMOS sensor [33] is 13% lower, on average, than the MTF of the 22.5 μm CMOS sensor (investigated in the present study) in the frequency range from 0 to 5 cycles/mm. In the higher spatial frequency range (5–10 cycles/mm), the MTF values differ by 2% on average. To explain these differences the combined effects of screen thickness/sensor pixel size, as well as the screen optical properties must be taken into account. The screen of our system is slightly thicker (65.1 mg/cm^2 instead of 59.2 mg/cm^2) and, in addition, it has not been optically optimized (i.e., incorporation of special light absorbing dyes) like commercially available screens. However, taking into account our results, it could be claimed that the red phosphor based system can show improved or acceptable signal transfer properties in the whole spatial frequency range.

Fig. 6 shows a comparison between the MTF of the Radeye HR CMOS sensor under investigation combined with the 33.3 mg/cm^2 Gd_2O_2S:Eu screen and a previously published MTF of the same sensor coupled to a 33.9 mg/cm^2 Gd_2O_2S:Tb screen [31] under 28 kVp X-ray spectrum. The MTFs of the CMOS/33.3 mg/cm^2 Gd_2O_2S:Eu screen combination are comparable to the previously published MTF of the CMOS/33.9 mg/cm^2 Gd_2O_2S:Tb screen combination [30].

Figs. 7 and 8 show extracted 1D normalized noise-power spectra (NNPS), for the u direction, obtained from uniformly exposed images under RQA5 and W/Rh conditions. NNPS shows variation over a large spatial frequency range. For example, a decrease from 7.62×10^{-6} mm^2 down to 1.29×10^{-6} mm^2 was observed in NNPS values in the range from 2 to 5 cycles/mm (exposure level 11.2 μGy for the RQA 5 beam quality). In the W/Rh beam quality (exposure level 167.0 μGy) a decrease of 70% was observed. This is attributed to the fact that in the CMOS system, a 2D correction is applied reducing the structured noise in each image. In the medium to high frequency range, the noise levels of

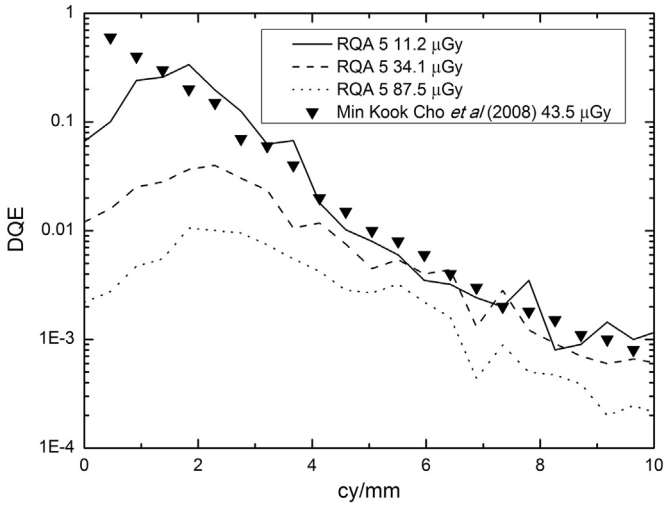

Fig. 9. Comparison of the DQE curves between the CMOS/Gd_2O_2S:Eu 65.1 mg/cm^2 sensor under investigation and a previously published CMOS/Gd_2O_2S:Tb 59.2 mg/cm^2 sensor under RQA 5 beam quality.

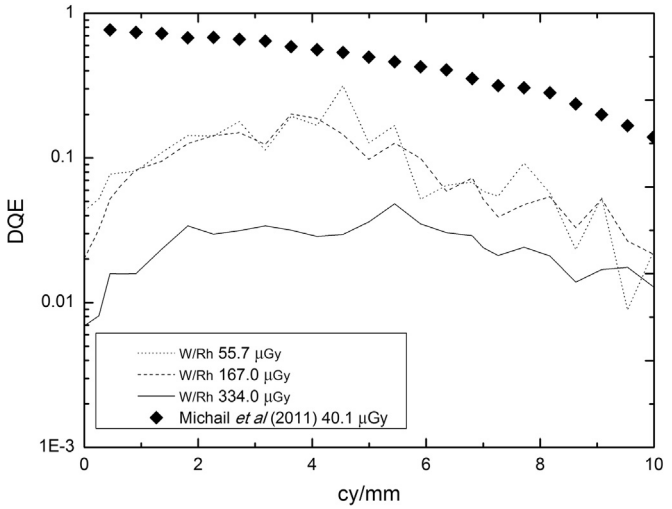

Fig. 10. Comparison of the DQE curves between the CMOS/Gd_2O_2S:Eu 33.3 mg/cm^2 sensor under investigation and a previously published CMOS/Gd_2O_2S:Tb 33.9 mg/cm^2 sensor under W/Rh and RQA M2 beam qualities, respectively.

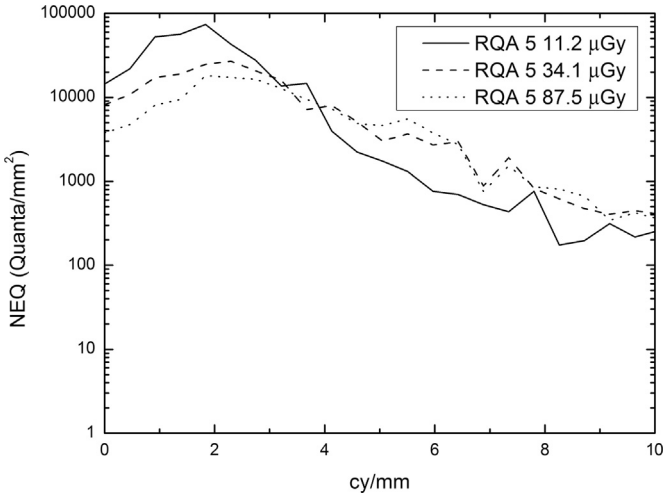

Fig. 11. NEQ curves for the RQA 5 beam quality.

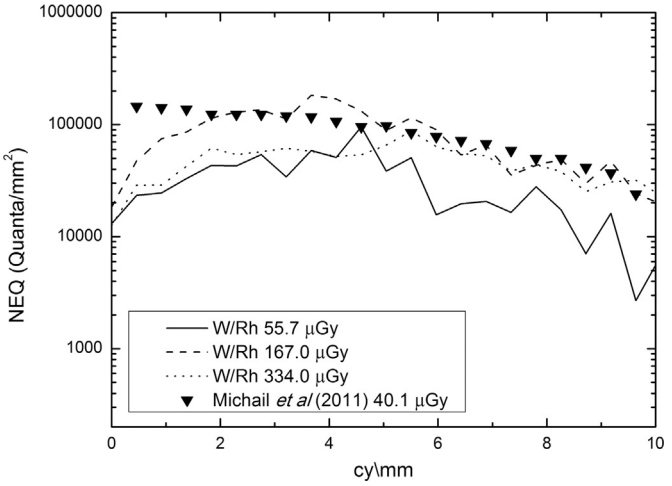

Fig. 12. Comparison of the NEQ curves between the CMOS/Gd_2O_2S:Eu 33.3 mg/cm^2 sensor under investigation and a previously published CMOS/Gd_2O_2S:Tb 33.9 mg/cm^2 sensor under W/Rh and RQA M2 beam qualities, respectively.

the image are related to the MTF of the system. The rather slow variation of the NNPS may be attributed to the fact that MTF remains high in this frequency range. For comparison purposes, NNPS of a CMOS sensor coupled to a Gd_2O_2S:Tb screen of 59.2 mg/cm^2 coating thickness measured in a previous study is also shown in Fig. 7 [32]. This curve was obtained from a 48 μm passive pixel sensor under the representative RQA 5 beam quality, at an exposure level of 43.5 μGy. Fig. 7 shows that the noise levels of the CMOS sensor under investigation is higher than that of the previously published study [33], due to the smaller pixel size of the CMOS sensor under investigation leading to lower photon collection efficiency and to a subsequent decrease in the signal to noise ratio (SNR) [68,69].

An additional comparison for the 28 kVp is shown in Fig. 8 in which the NNPS of the CMOS sensor under investigation, coupled to a commercial Gd_2O_2S:Tb screen of 33.9 mg/cm^2 coating thickness measured in a previous publication of our group is also shown for comparison purposes [31]. This curve was obtained under the representative RQA M2 (Mo/Mo at 28 KV) beam quality at exposure level of 40.1 μGy [30]. NNPS of the CMOS sensor/Gd_2O_2S:Eu screens combination shows higher noise in the whole spatial frequency range. The reduced NNPS values of Ref. 30 can be attributed to the lower energy components of the RQA M2 used in that study, which increase the X-ray quantum detection efficiency (QDE). This enhances the X-ray absorption properties of Gd_2O_2S, due to the fact that lower energy photons can be better absorbed, resulting in lower noise values.

Figs. 9 and 10 show DQE curves for the RQA 5, and W/Rh qualities, obtained according to (3). DQE was investigated at various air kerma settings at the detector surface. DQE decreases as the ESAK increases due to the influence of the NNPS and MTF. All the DQE curves show an increase in the spatial frequency from 0 to 1.8 cycles/mm for the RQA 5 and from 0 to 5 cycles/mm for the W/Rh. This is due to the fact that NNPS falls off rapidly in these spatial frequency ranges. Thereafter the reduction rate of the NNPS falls off in contrast with the corresponding of the MTF curves, contributing to a decrease in the DQE. The uncertainly of DQE values is lower than 10%, which is within the relative error limits suggested by IEC [32] since the relative error in MTF and NNPS calculations is 1% and 4% respectively. For comparison purposes, DQE of the 48 μm pixel size CMOS sensor [33] (RQA 5) at an exposure level of 43.5 μGy is also shown in Fig. 9. The DQE values of the previously published study [33] were higher in the low

spatial frequency range (up to 1.8 cycles/mm). This is due to the higher NNPS values of this spatial frequency range of the detector under investigation which contributes to lower DQE values. Thereafter DQE curve is comparable in the whole spatial frequency range due to the combined effects of MTF, NNPS and incident X-ray spectra, as depicted in the previous figures.

In Fig. 10, DQE curves, of the CMOS sensor under investigation, coupled to a commercial Gd_2O_2S:Tb screen, published in a previous study, is also shown for comparison purposes, under RQA M2 conditions, at an exposure level of 40.1 μGy [31]. DQE values of the currently investigated CMOS sensor/scintillating screen combination is lower than the corresponding of the CMOS/Gd_2O_2S:Tb screen combination [31], due to the higher noise performance of the current CMOS/Gd_2O_2S:Eu for the reasons previously reported.

Figs. 11 and 12 show noise equivalent quanta (NEQ) of the RQA 5 and W/Rh beam quality, calculated from the MTF, NNPS and the measured X-ray photon distribution at the detector surface. The shapes of the NEQ curves are affected by both NNPS and MTF. The amplitude of NEQ is affected by the number of X-ray photons at the surface of the detector (photons/mm^2). As shown in these Figs., NEQ reaches a maximum (73,563 mm^{-2}) in the low frequency range (1.8 cycles/mm), under the RQA 5 (ESAK: 11.2 μGy) conditions and in the medium frequency range (183,074 mm^{-2} at 3.6 cycles/mm) under W/Rh conditions (ESAK: 167.0 μGy). In Fig. 12 NEQ values of a previously published CMOS/Gd_2O_2S:Tb sensor is also shown for comparison purposes [31]. NEQ values of this CMOS sensor is higher in the spatial frequency range up to 1 cycles/mm. NEQ curves of both CMOS sensors are comparable thereafter.

In Fig. 13 the information capacity values for the RQA 5 and W/Rh X-ray spectra, as a function of air kerma are shown. CMOS sensor/Gd_2O_2S:Eu screens combinations show higher IC values in the W/Rh energy level (2535–2747 bits/mm^2), in comparison to the RQA 5 (1730–1851 bits/mm^2) due to the higher MTF and incident air kerma values. These data show that, for a given level of incident X-ray fluence, information capacity is mainly determined by the intrinsic phosphor material properties and by the screen thickness of the system. At thick screens the lateral light trajectories are very long causing a large fraction of the laterally directed photons to be absorbed before reaching the screen output. As expected, information capacity increased with increasing air kerma values. Furthermore, for high air kerma values information capacity showed a tendency to saturate. This could grant an index of how a digital imaging system takes advantage of the increasing SNR. In Fig. 13 IC values of a CMOS sensor/Gd_2O_2S:Tb screen combination, studied under RQA M2 beam quality are also shown. The IC of this system show an almost proportional increase to air kerma values in comparison with the current CMOS/Gd_2O_2S:Eu. This is due to the lower air kerma values that gave the RQA M2 beam quality, suggesting that a higher air kerma increases the imaging information. The practical value of the IC is that it defines an imaging performance index that evaluates image information

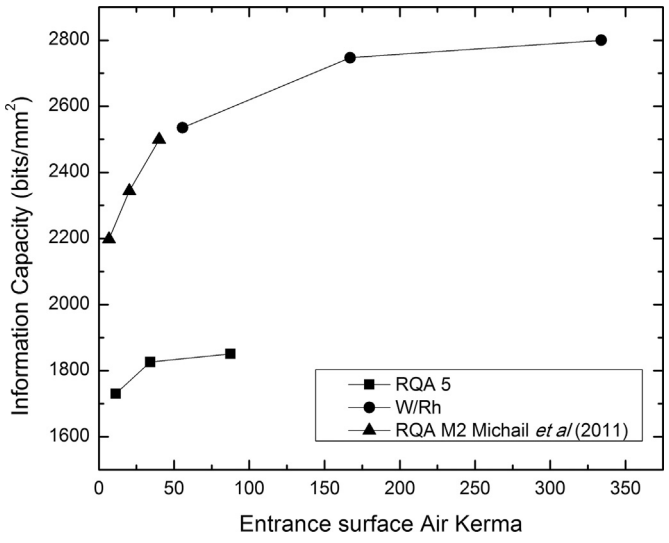

Fig. 13. IC values as a function of air kerma of the CMOS/Gd_2O_2S:Eu 65.1 mg/cm^2 and 33.3 mg/cm^2 sensors under RQA 5 and W/Rh beam qualities, respectively and the previously published CMOS/Gd_2O_2S:Tb 33.9 mg/cm^2 sensor under RQA M2 beam quality.

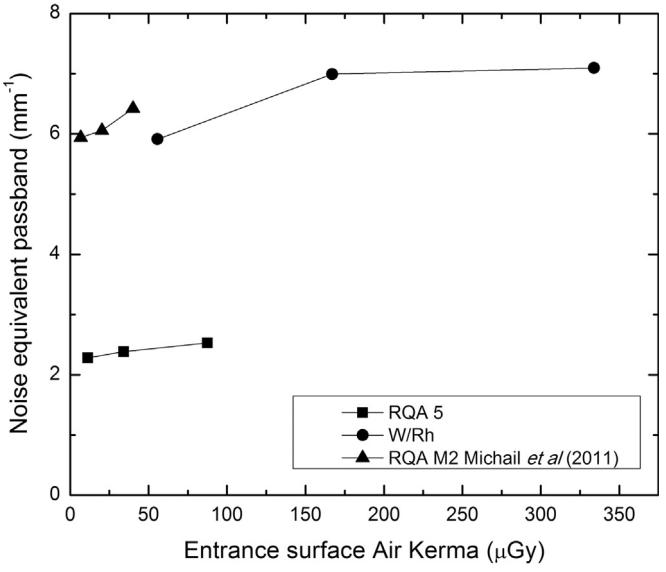

Fig. 14. Ne values as a function of air kerma of the CMOS/Gd_2O_2S:Eu 65.1 mg/cm^2 and 33.3 mg/cm^2 sensors under RQA 5 and W/Rh beam qualities, respectively and the previously published CMOS/Gd_2O_2S:Tb 33.9 mg/cm^2 sensor under RQA M2 beam quality.

Table 2
IC and Ne values for the RQA 5 and W/Rh beam qualities.

Beam quality	Entrance surface air-kerma (ESAK; μGy)	Information capacity (bits/mm^2)	Noise equivalent passband (mm^{-1})
RQA M2 [31]	65.8 ± 0.03	2475 ± 25	5.93 ± 0.06
	197.4 ± 0.07	2678 ± 27	6.05 ± 0.06
	394.1 ± 0.08	2733 ± 27	6.42 ± 0.06
(W/Rh)	55.7 ± 0.03	2535 ± 27	5.91 ± 0.06
	167.0 ± 0.06	2747 ± 27	6.99 ± 0.07
	334.0 ± 0.07	2821 ± 28	7.09 ± 0.07
RQA 5	11.2 ± 0.02	1730 ± 17	2.28 ± 0.02
	34.1 ± 0.03	1826 ± 18	2.38 ± 0.02
	87.5 ± 0.05	1851 ± 19	2.52 ± 0.03

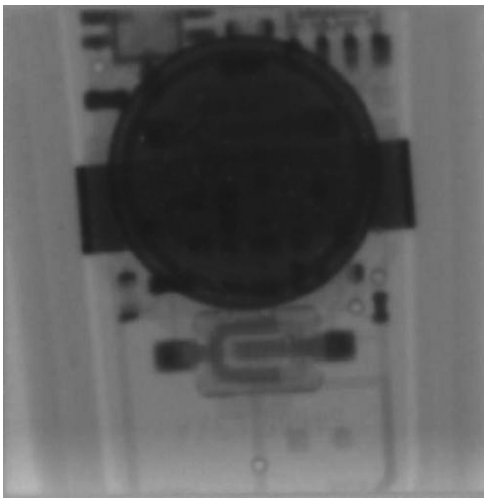

Fig. 15. Image obtained from the CMOS/Gd_2O_2S:Eu combination at 74 KVp with 21 mm Al filtration.

quantity by a single numerical value. Information capacity is not expressed for specific frequency values since it is the outcome of integrating over the spatial frequency bandwidth [70]. As the allowed spatial frequency region is enlarged to include higher and higher spatial frequencies, the information capacity slightly increase at fixed SNR. This is because in high frequencies the pixels of the detector are noisier and have, thus, a lower capacity to carry information.

In Fig. 14 the noise equivalent passband values for the RQA 5 and W/Rh as a function of air kerma are shown. CMOS/Gd_2O_2S:Eu screen combinations show higher Ne values in the W/Rh energy level (5.91–7.09 mm^{-1}), in comparison to the RQA 5 energy range (2.28–2.52 mm^{-1}) due to the higher MTF values and to the screen thickness. This behavior is due to the increasing effect of lateral light spread as screen thickness increase, which induces image sharpness degradation. Ne shows a tendency to saturate with increasing air kerma values. The Ne values of CMOS/Gd_2O_2S:Tb combination of the previous study show an proportional increase to air kerma values, in contrast with the current CMOS sensor, due to the lower air kerma values of RQA M2 beam quality. At low air kerma values of both CMOS sensors (CMOS/Gd_2O_2S:Eu and CMOS/Gd_2O_2S:Tb) at 28 kVp the Ne values are very close. Although MTF curves are different the same Ne values are equivalent with respect to the white noise. Table 2 shows the IC and Ne values for RQA 5 and W/Rh beam quality.

Fig. 15 shows an initial image of a simple electronic device obtained from the CMOS/Gd_2O_2S:Eu sensor screen combination under the RQA 5 beam quality (obtained at 74 KVp with 21 mm Al filtration). This image demonstrates, that the use of a CMOS/Gd_2O_2S:Eu sensor screen combination may be practically feasible.

4. Conclusion

In the present study the information content of a high resolution CMOS based imaging sensor combined with custom made europium activated Gd_2O_2S screens was investigated in terms of the information capacity (IC) and the noise equivalent passband (Ne). Experimental determination of the spatial frequency dependent modulation transfer function (MTF), normalized noise power spectrum (NNPS), detective quantum efficiency (DQE) and noise equivalent quanta (NEQ) at 70 and 28 kVp was implemented in order to assess the single index image information content parameters. Results showed that the red emitting phosphor/CMOS sensor combination has comparable image quality parameters results in terms of MTF, NNPS, DQE and NEQ compared to previously published data for terbium activated Gd_2O_2S/CMOS sensor combinations. The information capacity and the noise equivalent passband were found with high values suggesting an acceptable imaging performance in terms of information content and sharpness. Since the imaging performance of europium activated Gd_2O_2S screens, combined to CMOS sensors was found comparable to that of terbium activated Gd_2O_2S screens, red emitting phosphors could be used in digital imaging systems, where the Si based photodetectors are more sensitive to longer wavelength ranges, and particularly in the red wavelength range.

Acknowledgments

This research has been co-funded by the European Union (European Social Fund) and Greek national resources under the framework of the “Archimedes III: Funding of Research Groups in TEI of Athens” project of the “Education & Lifelong Learning” Operational Programme.

Authors wish to thank Dr. Nickolas Marshall for the offer of the OBj_IQ software.

References

[1] J.T. Dobbins III, D.J. Godfrey, Physics in Medicine and Biology 48 (2003) R65.
[2] R.E. Alvarez, J.A. Seibert, S.K. Thomson, Medical Physics 31 (3) (2004) 556.
[3] J.G. Mainprize, N.L. Ford, S. Yin, E.E. Gordon, W.J. Hamilton, T.O. Tumer, M.J. Yaffe, Medical Physics 29 (12) (2002) 2767.
[4] G. Patatoukas, A. Gaitanis, N. Kalivas, P. Liaparinos, D. Nikolopoulos, A. Konstandinidis, I. Kandarakis, D. Cavouras, G. Panayiotakis, Nuclear Instruments and Methods in Physics Research Section A 569 (2006) 260.
[5] R.E. Alvarez, Medical Physics 37 (2010) 822.
[6] L.E. Antonuk, Q. Zhao, Y. El-Mohri, H. Du, Y. Wang, R.A. Street, J. Ho, R. Weisfield, W. Yao, Medical Physics 36 (7) (2009) 3322.
[7] M. Nikl, Measurement Science and Technology 17 (2006) R37.
[8] H.G. Chotas, J.T. Dobbins III, C.E. Ravin, Radiology 210 (1999) 595.
[9] H.K. Kim, G. Cho, S.W. Lee, Y.H. Shin, H.S. Cho, Measurement Science and Technology 48 (3) (2001) 662.
[10] M. Bigas, E. Cabruja, J. Forest, J. Salvi, Microelectronics 37 (2006) 433.
[11] H.K. Kim, J.K. Ahn, G. Cho, Nuclear Instruments and Methods in Physics Research Section A 545 (2005) 210.
[12] A.M. Gurwich, Radiation Measurements 24 (1995) 325.
[13] J.A. Rowlands, J. Yorkston, Flat Panel Detectors for Digital Radiography, in: J. Beutel, H.L. Kundel, R.L. Van Metter (Eds.), Handbook of Medical Imaging: Physics and Psychophysics, vol. 1, SPIE, Bellingham, WA, 2000, pp. 223–313 (Chapter 4).
[14] AN10: QE Measurements of the RadEye1 Image Sensor Document Library, Rad-icon Imaging Corporation a division of Dalsa, Sunnyvale, CA, 2006. Available from: ⟨http://www.rad-icon.com/pdf/Radicon_AN10.pdf⟩.
[15] P.A. Rodnyi, S.B. Mikhrin, A.N. Mishin, A.V. Sidorenko, IEEE Transactions on Nuclear Science NS48 (2001) 2340.
[16] E. Zych, Spectroscopy of Eu-activated Lu_2O_3 X-ray phosphors, in: O.T. Chang (Ed.), Frontal Semiconductor Research, Nova Science, New York, 2006, pp. 1–24.
[17] M. Nikl, Measurement Science and Technology 17 (2006) R37.
[18] C.M. Michail, I.G. Valais, A.E. Toutountzis, N.E. Kalyvas, G.P. Fountos, S.L. David, I.S. Kandarakis, G.S. Panayiotakis, IEEE Transactions on Nuclear Science NS55 (2008) 3703.
[19] C.M. Michail, G.P. Fountos, P.F. Liaparinos, N.E. Kalyvas, I. Valais, I.S. Kandarakis, G.S. Panayiotakis, Medical Physics 37 (2010) 3694.
[20] C.M. Michail, G.P. Fountos, I.G. Valais, N.I. Kalyvas, P.F. Liaparinos, I.S. Kandarakis, G.S. Panayiotakis, IEEE Transactions on Nuclear Science NS58 (2011) 2503.
[21] A. Wiatrowska, E. Zych, L. Kepinski, Radiation Measurements 45 (2010) 493.
[22] A. Lempicki, C. Brecher, P. Szupryczynski, H. Lingertat, V. Nagarkar, S.V. Tipnis, S.R. Miller, Nuclear Instruments and Methods in Physics Research Section A 488 (2002) 579.
[23] V.V. Nagarkar, S.V. Tipnis, S.R. Miller, A. Lempicki, C. Brecher, P. Szupryczynski, H. Lingertat, IEEE Transactions on Nuclear Science NS50 (2003) 297.
[24] J.M. Boone, M. Tecotzky, G.M. Alexander, Radiology 183 (1992) 863.
[25] M. Gambaccini, A. Taibi, A. Del Guerra, M. Marziani, A. Tuffanelli, Physics in Medicine and Biology 41 (1996) 2799.
[26] A. Taibi, A. Del Guerra, M. Gambaccini, M. Marziani, A. Tuffanelli, Nuclear Instruments and Methods in Physics Research Section A 392 (1997) 210.
[27] M. Gambaccini, A. Taibi, P. Baldelli, A. Del Guerra, A. Tuffanelli, Nuclear Instruments and Methods in Physics Research Section A 409 (1998) 508.
[28] E.J. Harris, G.J. Royle, R.D. Speller, J.A. Griffiths, G. Kidane, A.M. Hanby, Nuclear Instruments and Methods in Physics Research Section A 513 (2003) 27.

[29] C.M. Carpenter, G. Pratx, C. Sun, L. Xing, Physics in Medicine and Biology 56 (2011) 3487.
[30] C.M. Carpenter, G. Pratx, C. Sun, R. Rao, L. Xing, Medical Physics 37 (8) (2010) 4011.
[31] C.M. Michail, V.A. Spyropoulou, G.P. Fountos, N.I. Kalyvas, I.G. Valais, I.S. Kandarakis, G.S. Panayiotakis, IEEE Transactions on Nuclear Science NS58 (1) (2011) 314.
[32] Medical Electrical Equipment—Characteristics of Digital X-Ray Imaging Devices, Determination of the Detective Quantum Efficiency-Mammography Detectors, IEC, International Electrotechnical Commission, Geneva, Switzerland, IEC 62220-1-2 (2005).
[33] M.K. Cho, H.K. Kim, T. Graeve, S.M. Yun, C.H. Lim, H. Cho, J.M. Kim, IEEE Transactions on Nuclear Science NS55 (3) (2008) 1338.
[34] G.E. Giakoumakis, C.D. Nomicos, E.N. Yiakoumakis, E.K. Evangelou, Physics in Medicine and Biology 35 (1990) 1017.
[35] M. Sadowsky, Journal of the Electrochemical Society 95 (1949) 112.
[36] S. Shigeo, M. Yen William, Phosphor Handbook, CRC, New York576.
[37] Remote RadEye Systems Rad-icon Imaging Corporation a division of Dalsa, Sunnyvale, CA. Available from: ⟨http://www.rad-icon.com/products-remote.php⟩.
[38] Selenia Digital Mammography. Available from: ⟨http://www.hologic.com/en/breast-imaging/digital-mammography/selenia/⟩.
[39] Del Medical Systems Group, Roselle, IL. Available from: ⟨http://www.delmedical.com⟩.
[40] X-ray & Gamma Ray Detector, XR-100T-CdTe, Amptek, Bedford, MA. Available from: ⟨http://www.amptek.com/xr100cdt.html⟩.
[41] L. Abbene, A.L. Manna, F. Fauci, G. Gerardi, S. Stumbo, G. Raso, Nuclear Instruments and Methods in Physics Research Section A 571 (2007) 373.
[42] J.R. Greening, Fundamentals of Radiation Dosimetry, Institute of Physics, London, UK56.
[43] U. Neitzel, S. Gunther-Kohfahl, G. Borasi, E. Samei, Med. Phys. 31 (2004) 2205.
[44] E. Samei, M.J. Flynn, D.A. Reimann, Medical Physics 25 (1998) 102.
[45] N.W. Marshall, Physics in Medicine and Biology 51 (2006) 2441.
[46] J.T. Dobbins III, Image quality metrics for digital systems, in: J. Beutel, H.L. Kundel, R.L. Van Metter (Eds.), Handbook of Medical Imaging: Physics and Psychophysics, vol. 1, SPIE, Bellingham, WA, 2000, pp. 161–222.
[47] H. Illers, E. Buhr, C. Hoeschen, Radiation Protection Dosimetry 114 (1–3) (2005) 39.
[48] R.E. Hendrick, E.D. Pisano, A. Averbukh, C. Moran, E.A. Berns, M.J. Yaffe, B. Herman, S. Acharyya, C. Gatsonis, American Journal Of Roentgenology 194 (2010) 362.
[49] J.M. Boone, Medical Physics 28 (3) (2001) 356.
[50] R. Shaw, Reports on Progress in Physics 41 (1978) 1103.
[51] R.F. Wagner, D.G. Brown, M.S. Paster, Medical Physics 6 (1979) 83.
[52] J.C. Dainty, R. Shaw, Image Science, Academic Press, New York232–380.
[53] C.E. Shannon, Bell System Technical Journal 27 (1948) 379.
[54] R.C. Jones, Journal of the Optical Society of America A 50 (1961) 1166.
[55] R.C. Jones, Journal of the Optical Society of America A 52 (1962) 1193.
[56] H. Kanamori, Japanese Journal of Applied Physics 7 (1968) 414.
[57] M.A. Maiorchuk, V.V. Nikitin, V.D. Samoilov, Soviet Journal of Quantum Electronics 4 (2) (1974) 168.
[58] D.G. Brown, M.P. Anderson, R.F. Wagner, SPIE 206 (1979) 77.
[59] R. Shaw, Some modem aspects of image evaluation, in: A.G. Hags (Ed.), The Physics of Medical Imaging: Recording System, Measurements and Techniques, American Association of Physicists in Medicine, New York, 1979, pp. 515–523.
[60] A.L. Evans, in: Adam Hilger (Ed.), The Evaluation of Medical Images, 1981, pp. 45–46.
[61] H. Kanamori, M. Matsuoto, Physics in Medicine and Biology 29 (1984) 303.
[62] C.M. Michail, G.P. Fountos, S.L. David, I.G. Valais, A.E. Toutountzis, N.E. Kalyvas, I.S. Kandarakis, G.S. Panayiotakis, Measurement Science and Technology 20 (2009) 104008.
[63] E.C. Gregg, Journal of Nuclear Medicine 9 (1967) 116.
[64] R.F. Wagner, D.G. Brown, M.S. Paster, Medical Physics 6 (1979) 83.
[65] I. Kandarakis, D. Cavouras, G.S. Panayiotakis, C.D. Nomicos, Applied Physics B 72 (2001) 887.
[66] I. Kandarakis, D. Cavouras, G.S. Panayiotakis, C.D. Nomicos, Applied Radiation and Isotopes 52 (2000) 119.
[67] C.E. Shannon, Proceedings of the IEEE (1998) pp. 447–457.
[68] T. Chen, P.B. Catrysse, A. El Gamal, Brian A. Wandell, Proceedings of SPIE 3965 (2000) 451.
[69] J. Farrell, F. Xiao, S. Kavusi, Proceedings of SPIE Digital Photography II vol. 6069 (2006) pp. 60690N.
[70] C.M. Michail, Investigation of optical and imaging characteristics of fluorescent screens for use in digital imaging detectors suitable for telemedicine (Ph. D. Thesis) University of Patras, Greece (2010).